Time Domain Optical Coherence Tomography (OCT) for MEMS-based Endoscopic Application

Yunbo Liu

A thesis

submitted in partial fulfillment of the

requirements for the degree of

Master of Science

University of Washington

2014

Committee:

Lih Y. Lin

Ruikang Wang

Program Authorized to Offer Degree:

Electrical Engineering

University of Washington

Abstract

As an innovative bio-tissue imaging modality, Optical Coherence Tomography (OCT) endoscope remains attractive due to its high resolution, capability of subepithelial morphology imaging, compact size and low cost of system. Recently, a MEMS-based endoscope scanner is demonstrated to have the ability of focus-tracking and 2D lateral scanning. A time-domain OCT employing Rapid Scanning Optical Delay Line (RSOD) is constructed based on the need of this new MEMS scanner. The effect of dispersion compensation is discussed. An axial resolution of 20 μm and a lateral resolution of 30 μm is demonstrated.

Time Domain Optical Coherence Tomography (OCT) for MEMS-based Endoscopic Application

Yunbo Liu

Chair of the Supervisory Committee:

Dr. Lih Y. Lin

Electrical Engineering

Table of Content

Contents

Chapter 1 Introduction

1.1 Motivation

Despite the rapid development of biomedical imaging technologies, including X-ray Imaging, Ultrasound Imaging and Magnetic Resonance Imaging (MRI) that offer many advantages over different aspects, the need for a low-cost, real-time, soft tissue imaging remains. Conventional imaging methods are limited due to a variety of reasons when facing such a task. X-ray imaging has excellent depth of view. However, due to its short wavelength and therefore high photon energy, an incident photons will undergo inelastic scattering and transfer part of its energy to an outer shell electron of the tissue atom, therefore ionize the atom. The scattered photons will have a slightly longer wavelength and very likely it will undergo a direction similar to the original direction. This is called Compton scattering. Because of this, soft biological tissue is almost transparent under x-ray illumination [1]. Additionally, since x-ray imaging introduces ionizing radiation, it will lead to DNA double-strand breaks and cause damage to human body [2]. Ultrasound imaging provides a low-cost, fast imaging method for diagnosis in many areas of human body from valve motion, blood flow to liver metastases and neurovascular imaging. But Ultrasound imaging quality is fundamentally limited by its longer wavelength (0.77 mm – 0.1mm) compared to other imaging modalities [3]. MRI also provides excellent image depth for bio tissue. But the fact that MRI has poor resolution and it is bulky and expensive limits its application in clinical diagnosis [4]. Figure 1 shows the imaging depth and resolution for different imaging modalities. It is interesting to notice that Optical

Coherence Tomography (OCT) perfectly fills the gap between confocal microscopy and Ultrasound imaging [5]. Additionally, OCT systems are compact and capable of real-time imaging due to its fast scan rate. Its flexibility and convenience make it an ideal tool in clinical usage.

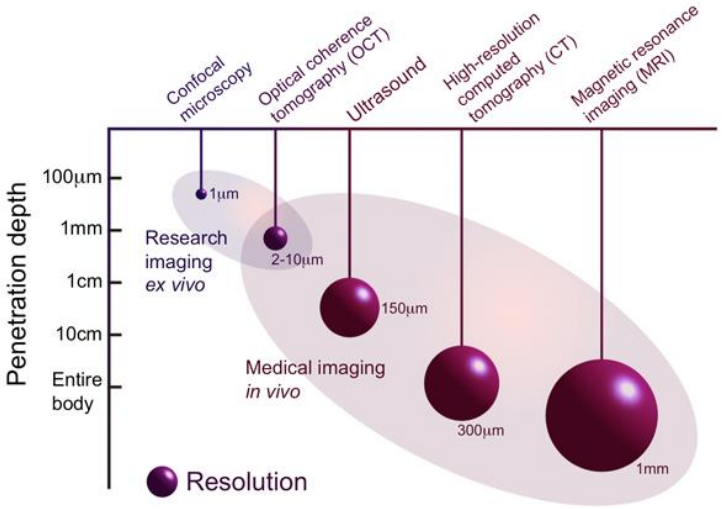

Figure 1. Different medical imaging modalities, penetration depth and resolution [5]

The flexibility of OCT is best proven by its combination with endoscopic imaging. Endoscopic imaging has been, and continuous to be important in clinical diagnosis. However, current clinical endoscope offers a magnified view of the epithelial surface but is not capable of imaging subepithelial morphology. Optical coherence tomography offers non-invasive in vivo assessment of tissue microanatomy below the epithelial surface in real time at resolutions (~0.5-10 μm) [6]. Since OCT system is compact compared to conventional imaging methods and it provides superior spatial and axial resolution, it is

ideal to combine it with endoscope to provide real-time, fast 3D tissue image of subepithelial morphology inside human body.

1.2 Association with MEMS micromirror

Beam scanning on the sample under imaging is required to form a spatial image using a focused laser beam. There are many different approaches for beam scanning for OCT systems. Piezoelectric fiber scanning is one of the commonly seen setup in which the optical fiber is attached to two sets of piezoelectric scanning actuators for 2D scanning [7]. However a piezoelectric actuation setup often suffers bulky imaging head due to the attached piezoelectric actuators around the fiber. Another common approach is microelectromechanical system (MEMS) micromirror beam scanner. This approach uses a micromirror that can rotate around its planer axes to achieve 2D scanning. Such mirror can be actuated either by a bimorph structure [8] or sets of comb drives [9].

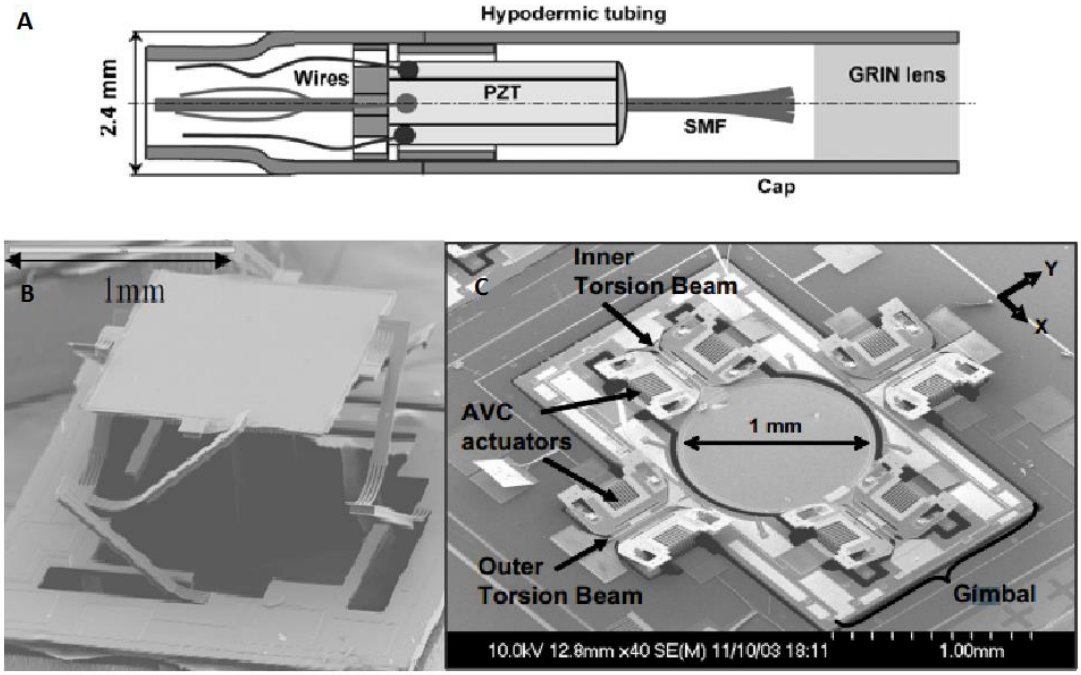

Figure 2. Piezoelectric-actuated scanning fiber endoscopy [7]. B. 2D bimorph scanning mirror [8]. C. 2D comb drive scanning mirror [9].

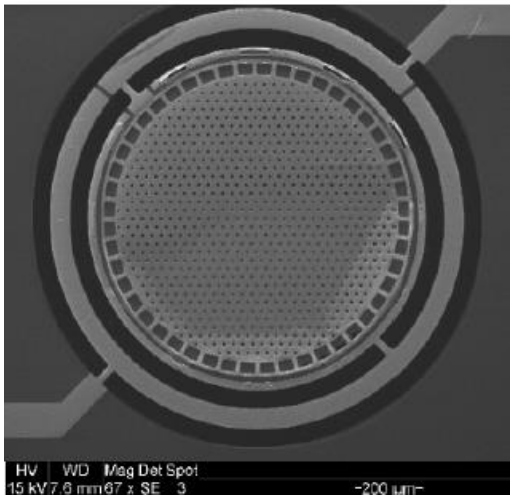

Figure 3. Dynamic focus-tracking 3D scanning mirror [6]

Although high resolution images have been demonstrated using above technologies [10-14], the large footprint of the actuation mechanisms makes an alternative MEMS-based miniature probe attractive. Additionally, both of the above solutions however, requires additional fixed optical lens to focus the light onto tissue. This focal length is usually fixed, thus in OCT applications, especially time-domain OCT (TD-OCT) the depth scanning image will suffer from signal deterioration due to the fact that the light is out of focus at some imaging depths. A recent new approach using electrostatic force actuation with dynamic focus-tracking MEMS scanning micromirror has been demonstrated to have the ability to maintain small device footprint due to the nature of electrostatic actuation while capable of deforming the mirror membrane to change the focal length [6]. Such mirror essentially performs as a reflecting mirror as well as a lens of tunable focal length. We believe that combining it with TD-OCT will improve the axial resolution of the images.

Chapter 2 Prior Arts

2.1 Ultrasound Imaging

There are many ways of understanding OCT, one of the most common way is to compare it to the ultrasound imaging. Since the development of first real-time scanner in 1970s, medical ultrasound imaging has become a mature and widely-used imaging modality. As stated above, ultrasound imaging has moderate image resolution and moderate penetration depth with real-time, fast imaging speed. Sound wave travels through biological tissue by alternately compressing and decompressing tissue. As sound wave

travels, it is affected by acoustic impedance analogous to electric current and impedance. Acoustic impedance is defined as

$$Z = \rho * c \tag{1}$$

where ρ is tissue density and c is sound velocity.

When sound wave encounters a region with different acoustic impedance, part of the wave will be reflected. Depending on the size of the tissue structure compared to sound wavelength, sound wave will go through directional reflection, or scattering. The reflection sound wave, or "echo", is picked up by transducers and converted to electric pulses. The time of flight of these returned waves depend on the depth of the tissue structures. These pulses will then be sent to computer. A line of dots will be generated and the position and intensity of each dot is determined by the time of the electric pulse and the amplitude of the pulse. Using above method, an anatomical image can be generated. A more interesting imaging class of ultrasound is the blood flow image in which the blood flow speed is measured by Doppler Effect. In such type of images, the velocity of a moving object inside biology tissue is measured by the frequency shift of the returned signal based on

$$F = Fo * \frac{v}{\frac{c}{2}} \tag{2}$$

where F is the Doppler shift frequency, F_o is the sound frequency in medium, v is the object flow speed and c is the speed of sound wave in tissue [15]. It is worth noting that such Doppler Effect is also utilized in OCT system, especially in heterodyne detection where a Doppler shift is generated by continuously changing the optical path length.

2.2 Michelson Interferometer

The basic principle of OCT originated from the Michelson interferometer, invented by Albert Abraham Michelson. A Michelson interferometer consists of two reflective mirror M1 and M2 shown in Figure 4. Light emitted by light source hits the beam splitter (usually a silvered mirror) at position A and half of the light will go through path 1 and reflected back to position C while the other half goes through optical path 2 and be reflected back to position C as well. These two light waves will interact with each other and be detected by the photodetector at position E. Depending on the length difference between optical path 1 and 2, either constructive or destructive interference will occur. Since both return beams will go through the beam splitter again, they lose 50% of their intensity. In some more complicated setup, a polarizing beam splitter and wave retarders can be used to avoid this power lost [6].

Assuming the light source is coherent, it can be represented by $U_1(r,t)=E_o\exp[i\phi_1(r)-wt]$ $U_1(r,t)=E_o\exp[i\phi_2(r)-wt]$. The intensity at position r after interference can be represented by

$$I \propto \left|Eo * e^{i(\varphi 1(r)-wt)} + Eo * e^{i(\varphi 2(r)-wt)}\right|^2 \quad (3)$$

$$I \propto Eo^2(\cos(\varphi 1 - wt) + \cos(\varphi 2 - wt))^2 + Eo^2(\sin(\varphi 1 - wt) + \sin(\varphi b2 - wt))^2 \quad (4)$$

$$I \propto 2 * Eo^2 + 2 * Eo^2 * \cos(\varphi 1 - \varphi 2) \quad (5)$$

Here the term $\varphi 1 - \varphi 2$ is the phase difference between two waves. When optical path ABC is equal to optical path ADC, the difference is zero. $I=4*E_o$^2, this is called

constructive interference. When ABC and ADC differs by half a wavelength, $\varphi 1 - \varphi 2 = \pi$, I=2*$E_o$^2-2*$E_o$^2 = 0, this is destructive interference. It is clear that, at constructive interference, the intensity level is 4 times higher than that of each individual optical path.

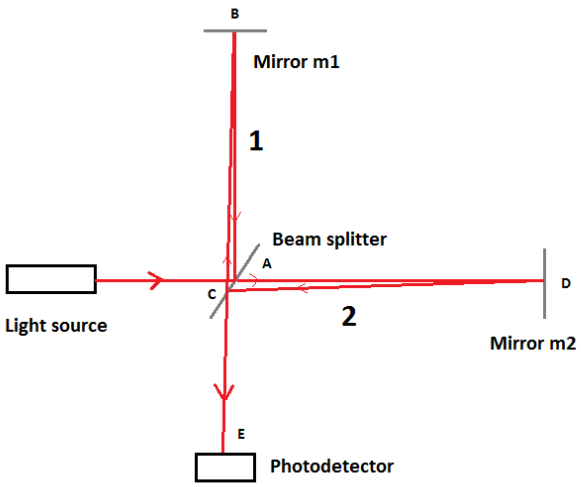

Figure 4. Schematic illustration of a Michelson interferometer

If one of the mirror, M1, for example, can be mechanically translated by more than a wavelength along optical path length 1, then the photodetector will see the signal level variation between constructive and destructive interference. This signal level variation due to optical path length difference forms the basis of the OCT technique.

Interference only happens within the coherence length of the light source, defined by $\mathrm{L} = \frac{4*\ln 2*\lambda^2}{\pi n*\Delta\lambda}$, where n is the refractive index of the medium and $\Delta\lambda$ is the spectrum width of the source. It is evident that an ideal monochromatic light source has an infinite coherence length since its bandwidth is 0. The larger the bandwidth, the shorter the coherence length. Therefore white light has only a very limited coherence length. As can

be seen later, in OCT application, a broadband, low-coherence light source is preferred to provide better axial resolution.

2.3 Low-coherence Reflectometry

One of the earlier application based on Michelson interferometer is the optical low-coherence reflectometry (OLCR) which appeared just a few years before OCT was first demonstrated. OLCR uses mode-locked laser emitting sub-picosecond pulses and a correlation detection based on second harmonic generation, or optical homodyne or heterodyne receivers. Using a setup very similar to the Michelson interferometer, OLCR employs a beam splitter to split the light source into a reference and an object arm. The backscattering light is recombined with the reference beam and the interference is detected by the detection system. The reference arm utilize an optical delay line consists of a translational mirror to investigate the depth information of the sample.

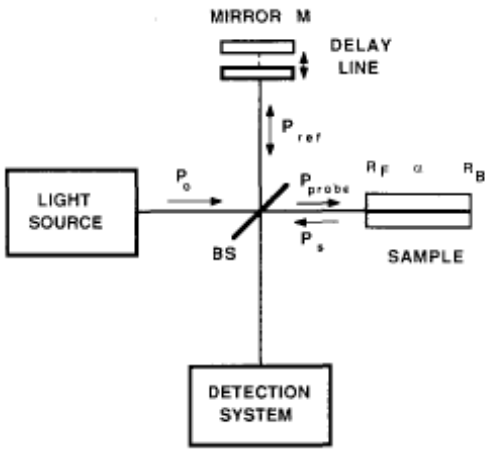

Figure 5. Schematic of OCLR. BS is the beam splitter. Rf and Rb are the front and end reflection coefficients and a is the average absorption coefficient of the sample. [17]

As can be seen in above figure, the OLCR has no spatial detection ability. It can only generate depth signal and it is often developed for diagnostics on fiber components, micro-optics and waveguide devices, for example, the length change of an optical fiber [17]. The operation principle of OLCR is however almost identical to OCT system as can be seen in later discussion.

Chapter 3 OCT Principle of Operation

3.1 Principle of operation

Analogous to ultrasonic pulse-echo imaging, OCT use low-coherence interferometry to produce a cross-sectional image of optical scattering from internal tissue microstructure [18]. The coherence property of light reflected from the tissue sample contains information on the time-of-flight delay from the reflective boundaries and backscattering sites in the sample. Such delay information is then used to determine the depth of these

boundaries and backscattering sites. Although the conventional confocal microscopy also have the ability to acquire depth information, the depth resolution (axial resolution) of OCT is not limited by numerical aperture but by the coherence length of the light source. Image axial resolution of 1-15 μm can be achieved [19]. Naturally, higher axial resolution is mainly limited by the bandwidth of the light source achievable at this moment [20].

The reflectivity of tissue under imaging is usually depth dependent due to changing of refractive index. Since imaging happens only at discrete depth of tissue the reflectivity ($R_{s1}=|r_{s1}|^2$) can be approximated also by discrete numbers r_{s1}, r_{s2} ... r_{sn} given by equation 6 below.

$$\mathrm{r_s(Z_s)} = \sum_{n=1}^{N} r_{sn}\, \delta(Z_s - Z_{sn}) \tag{6}$$

For the reference arm of OCT, the electric field can be express as

$$\mathrm{E_r} = \mathrm{E_o} * \mathrm{r} * \mathrm{e}^{\mathrm{i}*2\mathrm{kZ_r}} \tag{7}$$

Here r is the reflection coefficient of the mirror at the end of reference arm.

For sample arm of OCT, at depth Z_s, the electric field returning from sample can be expressed as

$$\mathrm{E_s} = \mathrm{E_o} * \sum_{n=1}^{N} r_{sn} * e^{i*2kZ_{sn}} \tag{8}$$

Here the constant 2 in exponential term in both equations represents the path of light the travels through the tissue/medium and comes back.

Current OCT system often use CCD image sensor as the detection element. The photocurrent I_D generated by the sensor is proportional to $|Er+Es|^2$.

$$|\mathrm{Er} + \mathrm{Es}|^2 = (\mathrm{Er} + \mathrm{Es}) * (\mathrm{Er} + \mathrm{Es})^* \tag{9}$$

$$|\mathrm{Er}+\mathrm{Es}|^2=\left(\mathrm{Eo}*\mathrm{r}*\mathrm{e}^{\mathrm{i}*2\mathrm{kZr}}+\ \mathrm{Eo}*\sum_{n=1}^{N}r_{sn}*e^{i*2kZsn}\right)*(\mathrm{Eo}*\mathrm{r}*\mathrm{e}^{-\mathrm{i}*2\mathrm{kZr}}+\ \mathrm{Eo}*\sum_{n=1}^{N}r_{sn}*e^{-i*2kZsn}) \quad (10)$$

$$|\mathrm{Er}+\mathrm{Es}|^2=Eo^2(r^2+r_{s1}^2+r_{s2}^2+\cdots+r_{sn}^2)+Eo^2r*\sum_{n=1}^{N}r_{sn}*\left(e^{i*2k(Zr-Zsn)}+e^{-i2k(Zr-Zsn)}\right)+Eo^2*\sum_{n\neq m=1}^{N}r_{sm}r_{sn}*\left(e^{i*2k(Zsn-Zsm)}+e^{-i2k(Zsn-Zsm)}\right) \quad (11)$$

$$|\mathrm{Er}+\mathrm{Es}|^2=Eo^2(r^2+r_{s1}^2+r_{s2}^2+\cdots+r_{sn}^2)+2Eo^2r\sum_{n=1}^{N}r_{sn}*\cos\left(2k(Zr-Zsn)\right)+2Eo^2\sum_{n\neq m=1}^{N}r_{sm}r_{sn}*\cos\left(2k(Z_{sn}-Z_{sm})\right) \quad (12)$$

In the above equation 12, the first term is an optical pathlength-independent component in the detector current. Its amplitude is proportional to the sum of the reflected light amplitude from both reference arm and object arm. This component is often called the "DC" component.

The second term is often called "cross-correlation". This term depend on both the light source wave number k and the pathlength difference $Zr-Zsn$ between the reference arm and object arm. Note that in the above equation, the reflectivity $R=r^2$. For biological tissues, reflectivity is usually on the order of 10^{-4} ~10^{-5} [21]. This is very small compare to the reflectivity in the reference arm, in which light often reflect off a mirror. Thus for most cases the returned reference field typically dominates the reflected sample field.

Analogous to cross-correlation, the third term is often referred to as "auto-correlation". The sample under imaging is approximated by discrete depths with different reflectivities.

Light reflected back from different depth will also interfere with each other if the path length difference is within a certain range. This range is coherence length. This term is usually undesired. However, from the above discussion for cross-correlation it is obvious to see that auto-correlation term is orders of magnitude smaller than the DC and cross-correlation terms. Thus, it is safe to ignore it in our discussion.

3.2 Lateral Resolution

The lateral resolution of an OCT system is no different from the lateral resolution of a conventional microscopy. The term resolution can be defined by Rayleigh Criterion as the distance between two diffraction peaks when the first diffraction minimum of one spot coincides with the maximum of another. This diffraction pattern is usually called Airy disk or Airy pattern, name after George Biddell Airy. Derived from the intensity profile of the Fraunhofer diffraction pattern of a circular aperture (the airy pattern), the first minimum of the diffraction pattern is achieved at k*a*sin(θ) where k is the wavenumber and a is the radius of the aperture. The solution of the Bessel function of the first kind at this minimum is k*a*sin(θ)=3.8317. So sin(θ)=3.8317*λ/(2π*a) ≈ 1.22*λ/D [22]. At small angle, the angular resolution can then be approximated by

$$\Delta\theta r = 1.22\frac{\lambda}{D} \tag{13}$$

Here D is the lens diameter and λ is the wavelength. The lateral resolution is then

$$\Delta x = 1.22 * f * \frac{\lambda}{D} \tag{14}$$

where f is the focal length of the lens used in the system.

Sometimes other definition of resolution can be seen in literature. For example, the Sparrow criterion, states that the resolution is the distance between two diffraction peaks where the two diffraction patterns overlaps at their half maximum position. It is easy to see that the Sparrow Criterion is a stricter criterion than the Rayleigh criterion [23]. It results in an angular resolution of

$$\Delta\theta r = 0.94\frac{\lambda}{D} \tag{15}$$

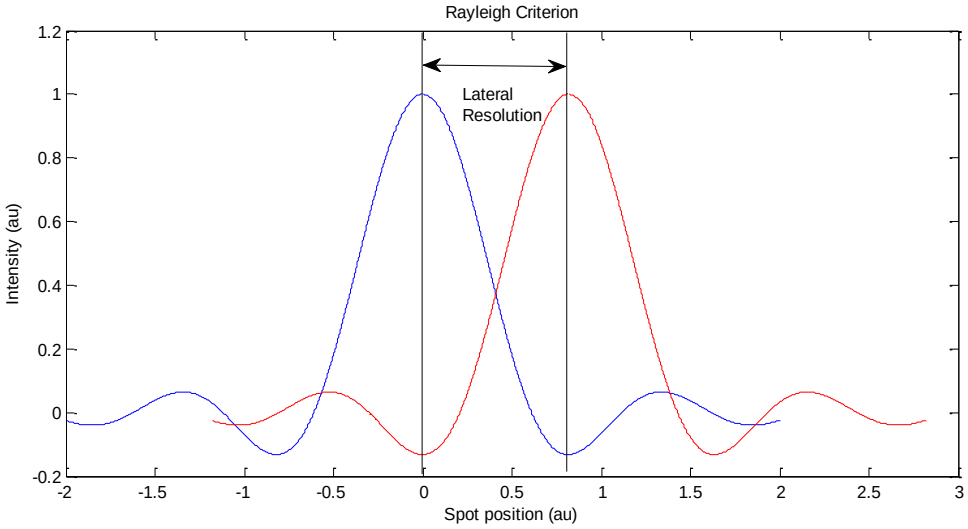

Figure 6. Rayleigh Criterion for lateral resolution

Applying either criterion results in a lateral resolution close to the wavelength of the light source used in the system. This is the fundamental limit of the system's lateral resolution. Similar to a confocal system, increasing the lateral resolution will result in a decrease in depth of focus.

3.3 Axial resolution

The axial resolution of the OCT system is determined by the coherence length of the light source. The auto-correlation is nonzero only within the coherence length, i.e. the spatial width of the auto-correlation is equal to the coherence length. The focused spot profile is assumed to be Gaussian in the sample arm by previous analyses [20]. In addition, the envelope of the field autocorrelation is equivalent to the Fourier transform of the power spectrum. Thus, the width of the autocorrelation function, or the axial resolution, is inversely proportional to the width of the power spectrum [24-26]. For a source with a Gaussian spectral distribution, the axial resolution can be expressed as

$$\Delta z = \left(2 * \frac{\ln 2}{\pi}\right) * \left(\frac{\lambda^2}{\Delta\lambda}\right) \tag{16}$$

where $\Delta\lambda$ is the full width at half maximum (FWHM) of the power spectrum and λ is the center wavelength. This equation is important for designing the OCT system. It specifies that the axial resolution is inversely proportional to the bandwidth of the light source. So high axial resolution could be achieved by using board band light source, such as a broadband laser diode. One advantage of OCT system can be seen from equation 14 and 16 is that the lateral and axial resolution are independent of each other. Thus high axial resolution can be achieved independent of the focusing condition of the lens. As a comparison, in conventional confocal microscopy, the depth of field is proportional to the inverse NA^2 [26]. It is obvious that the higher the lateral resolution, the smaller the depth of field.

As stated in the previous section, the coherence length of the optical system is $\mathrm{L} = \frac{4*\ln 2*\lambda^2}{\pi n*\Delta\lambda}$. For our OCT system, in air, the coherence length is calculated to be 15.4 μm. given center wavelength at 1325 nm and FWHM bandwidth of 100 nm.

3.4 Signal Processing and Noise Analysis

From the discussion for equation 12 in 3.1 we can see that the variation of the cross-correlation term in the detector is determined by the optical path length difference $Zr - Zsn$. This interference signal is usually very small compared to the DC signal. At any depth Zsn, with a fixed Zr distance, the cross-correlation term will simply be at a fixed signal level and the value will add up to the DC term. This will bring a major problem: for biological tissue, the interference signal will be overwhelmed by the DC term thus becoming undistinguishable. This issue can be solved by using optical heterodyne detection.

Optical heterodyne detection was adopted from radio frequency heterodyne circuits widely used from broadcast home receivers to transcontinental microwave systems. A heterodyne detector can be viewed as a two-step device: a converting stage that recovers the modulation frequency and the detection comes after the conversion stage [28].

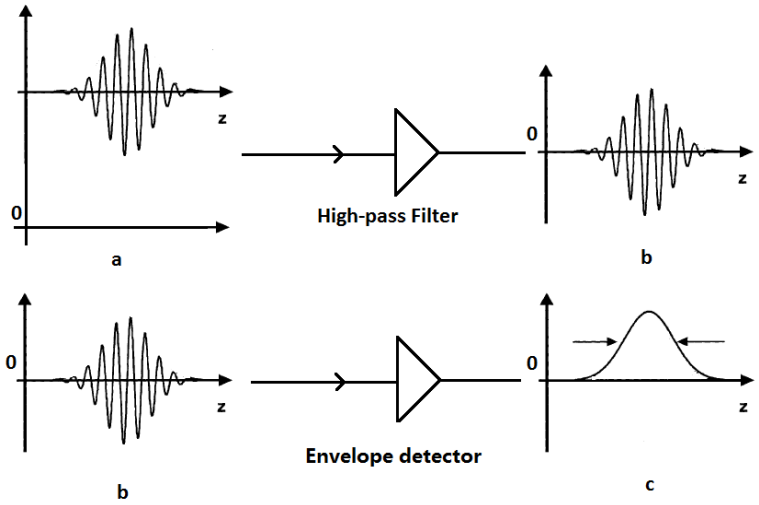

Figure 7. Signal processing flow of OCT signal. High-pass filter is used to eliminate the DC signal while low-pass-filter (an envelope detector in this case) is used to extract the information while increasing the system performance

The frequency modulation in OCT is usually accomplished by sweeping the reference arm optical path length Zr. Within the coherence length, this sweeping will generate a signal shown in Figure 7 a. Note that the interference signal is not centered on zero due to the DC component. This signal is then high-pass filtered to eliminate the DC component (Figure 7 b). An additional amplifier is usually employed after the high-pass filter since bio-tissues usually have very low reflectivity. To get the information of the biological tissue, this signal needs to be passed through an envelope detector to get the envelope of the amplitude. Doing this step using analog components instead of oversampling using computer will increase the picture generating speed. Depending on the demodulation characteristics, many OCT systems employ an extra modulator, such as a piezoelectric transducer [28] or an EO modulator [29] to provide a higher modulation frequency.

The AC signal is orders of magnitude lower than DC component (10^6 for biological tissue) thus it is crucial for the high-pass filter to remove the DC component completely without generating too much noise. Without the EO modulator, the cutoff frequency is fairly low. So a sharp cutoff, or a faster roll-off is desired for this system. The Chebyshev response is a mathematical strategy for achieving a faster roll-off by allowing ripple in the frequency response. Filters that apply this approach are called Chebyshev filters. Compare to other types of filters such as Butterworth filter, a Chebyshev filter has an increased attenuation in the stop band at the cost of passband ripples [30]. As can be seen later, a Chebyshev high-pass multiply-order active filter configuration gives very sharp and complete cutoff.

Figure 8 is a typical 2nd order Chebyshev type I high pass filter. Using ideal op amp approximation, the transfer function of this block can be easily obtained to be

$$\mathrm{G(s)} = \frac{\mathrm{s}^2 R1R2C}{\mathrm{s}^2\mathrm{R1R2C}^2+2\mathrm{sR2C}+1} \tag{17}$$

The cutoff frequency is then $\mathrm{f} = 2\pi \left|\frac{(-2*R2)-sqrt(4R1^2-4*R1R2)}{2R1R2}\right| Hz$. Thus resistance and capacitor value can be determined by the cutoff frequency.

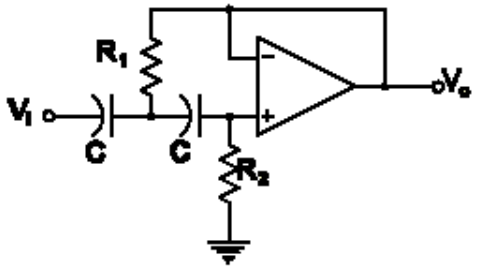

Figure 8. Second order Chebyshev high-pass active filter

There are four parameters needed to determine a Chebyshev filter: 1) pass band (high pass or low pass), 2) the cutoff frequency, 3) the allowed ripple in the passband and 4) the number of poles. At 400 Hz cutoff frequency, 1dB ripple, a five order Chebyshev high-pass filter is configured in figure 9. It is consist of a 1st order block and two 2nd order block. The Chebyshev polynomials are obtained from filter design handbook [30] and adjusted based on Multisim simulation results. The outputs after each block is simulated and shown in figure 10.

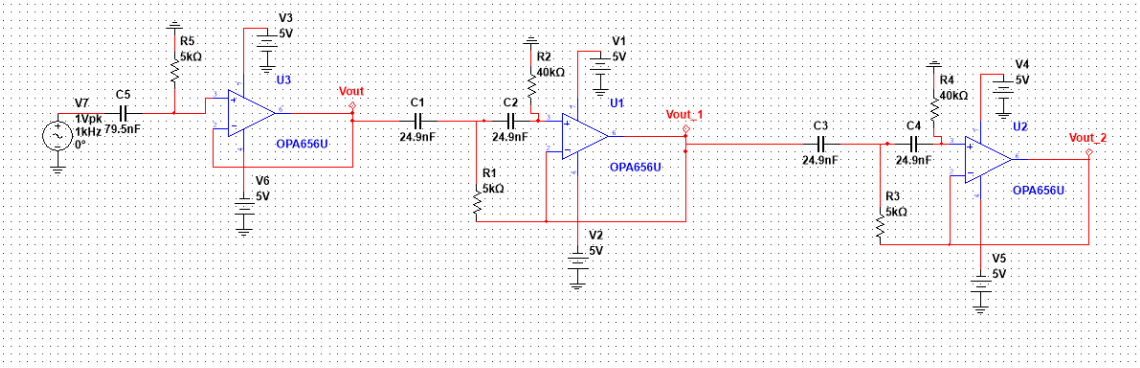

Figure 9. Circuit schematic of a 5th-order Chebyshev high-pass active filter

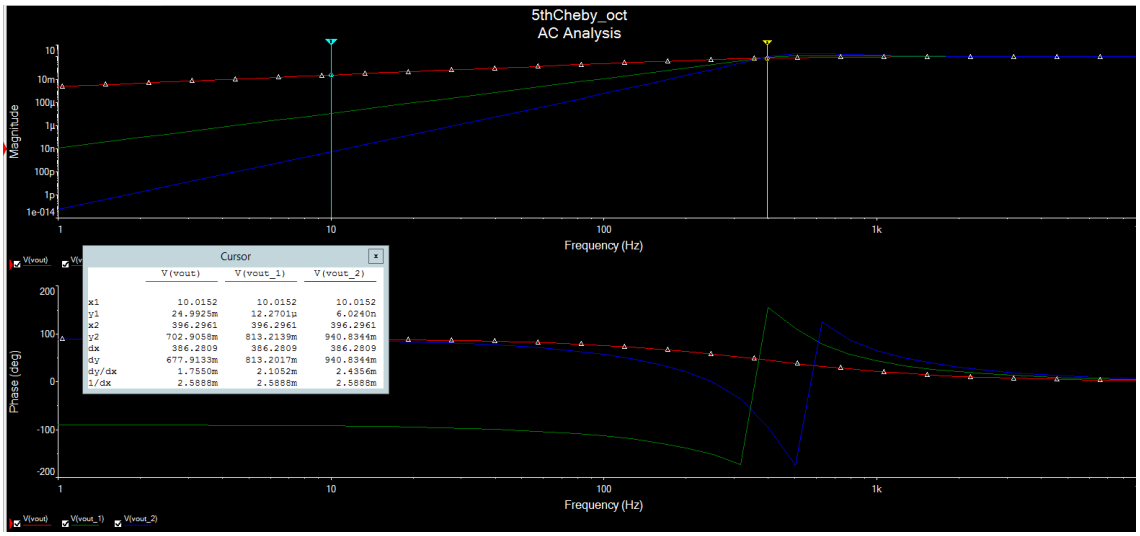

Figure 10. AC response of the 1st- (red), 3rd-(green) and 5th-order (blue) Chebyshev high-pass filter.

From the plot we can see for 5^{th} order configuration at 400 Hz, the gain is 940.8 mV compare to 6.024 nV at 10 Hz while for 1^{st} order configuration the gain is 24.9 mV. It is clear that higher order filter leaves much lower DC and low frequency component and a much faster roll-off. Additionally, the total noise at the output of the filter is simulated to be 602.3 nV. This is much lower than AC signal level. Simulation shows that 5^{th} order Chebyshev filter is suitable for our application.

The signal after the above hardware processing is then acquired by National Instrument PCI-6024E capable of 10k samples/second output and 200k samples/second input.

3.5 Optical Components

RSOD

Since constructive interference can only be achieved when the difference of the optical path between reference arm and object arm lies within the coherent length, OCT requires the scanning of the reference arm to achieve a group delay in order to acquire depth information from the sample tissue. In clinical applications, a fast imagine-acquisition rate is desirable. This requires a faster reference arm scanning rate. Such rapid-scanning optical delay (RSOD) was first developed using linear mechanical actuation. These methods often employ a galvanometer with a retroreflector mounted upon a lever arm that allows a small angle rotation to be converted into an optical path length delay. Scanning velocities of such systems are often limited by mechanical inertia to be

approximately 30 cm/s and the scanning rate is usually equal or less than 100 Hz. Moreover, they usually introduce delay-dependent dispersion [32].

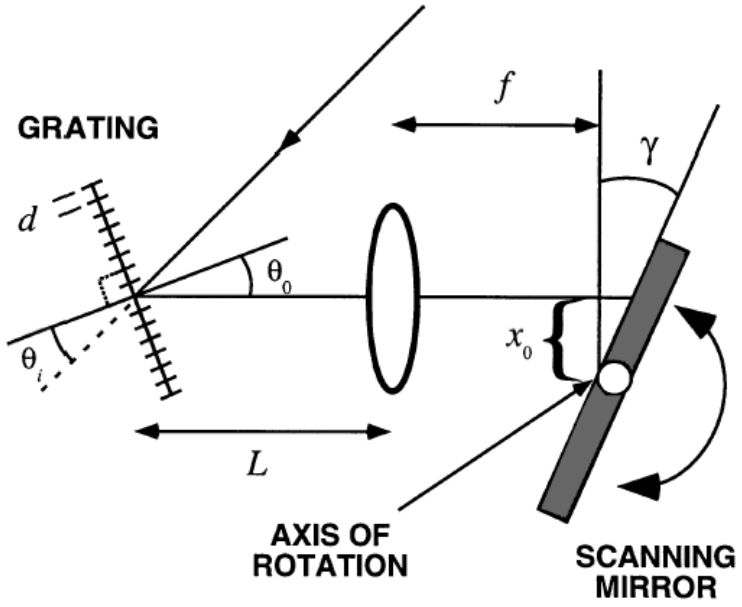

Figure 11. A schematic of RSOD, d is grating spacing, f is focal length, γ is galvanometer tilting angle [32]

A faster, grating-based RSOD used in femtosecond (fs) time-resolved signal-averaging measurement has been demonstrated to be capable of 500 Hz scanning rate with 50-100 fs range with only a total travel at the mirror edge of about 4 μm [32]. The operation of this RSOD is based on femtosecond Fourier-transform pulse shaping [33-36].

The grating in Figure 11 is a reflective type grating. Grating equation gives

$$\mathrm{d} * \sin \theta \mathrm{o} \ = m\lambda \tag{18}$$

Here d is the grating line spacing, θ_o is the diffraction angle and m is grating diffraction order. From (18),

$$\delta(\mathrm{d} * \sin\theta \mathrm{o}) = \mathrm{m} * \delta\lambda \tag{19}$$

$$\Delta\theta o = m * \frac{\Delta\lambda}{d * cos\theta o} \quad (20)$$

If we translate the angle difference in terms of vertical distance difference ΔX on the lens, equation 20 becomes

$$\Delta x = tan\Delta\theta o * f \quad (21)$$

where f is the focal length. Assuming the galvanometer has a small tilting angle of γ, the optical path length difference can then be expressed as

$$\Delta y = \gamma * \Delta x \quad (22)$$

Equation 20-22 simply states the fact that for a broadband laser source used in an OCT setup, different wavelengths correspond to different diffraction angles. The spectral component is displaced laterally with a difference of Δx. Such lateral distribution then causes different optical path length for different wavelengths upon the tilting of the reflection galvanometer. In Fourier optics, a lens can be viewed as a Fourier transform. After the light goes through the lens and hit the galvanometer, the result is the Fourier domain representation of the light multiplied by the phase ramp. This linear phase shift can be represented by

$$\varphi(w) = \left(4 * f * \frac{\pi}{d * cos\theta o}\right) * \left(\frac{w}{wo}\right) * \tan(\gamma) \quad (23)$$

Such linear phase shift corresponds to a time delay in the time domain. This will create the difference desired in optical path lengths among the two arms.

Another way to interpret this linear phase is to consider the group time delay. In signal processing, group delay is a measure of the time delay of the amplitude envelops of the signal of interests. Specifically, as light propagates through space, a medium, or certain devices consisting of different components, all frequency components of the signal are delayed. The signal will be distorted if different components undergo different amounts of delays. On the other hand, the signal will be the same after propagating through the device if the device is a linear phase device. Group delay is defined as

$$\tau g(w) = -\frac{d\varphi(w)}{dw} \tag{24}$$

$$\tau_g = \frac{d\varphi(\Omega)}{d\Omega} = \left[\frac{4f\pi}{wo*d}\cos(\theta o)\right] * \tan(\gamma) \tag{25}$$

From (25) it is obvious that passing through the RSOD will result in a time delay in the signal independent of the frequency and the overall signal is undistorted.

In our setup, we use a Richardson 53*-500R aluminum coated reflection grating with 5.4^O blaze angle and d=1/150mm=6.7 μm. It has over 80% efficiency at 1325 nm wavelength, which is suitable for our purpose. From Equation 1, the angle θ_o is calculated as 11.4^o given that the grating has spectral order m=1. The light source is a broadband superluminescent diode (SLD) with a center wavelength of 1325 nm and a full-width-half-maximum bandwidth of $\Delta\lambda = 100$ nm. Thus from equation 3, $\Delta\theta o$ calculated to be 0.0152 radian, or 0.8766 degree. This gives a vertical distance difference $\Delta x = \tan(0.0152) * 100\text{mm} = 1.52\text{mm}$ given the focal length of lens used is 100 mm. We use a Cambridge Technology 6210H Optical Scanner (galvanometer) which is capable of a rated angular

excursion of 10 degree mechanical angle or 20 degree optical angle under +-10V supply. Actuating at 1 V, the galvanometer will generate a mechanical angle of 1 degree. The difference in optical path length Δy is thus 26.5 μm. Using equation 25, the time delay τ_g = 2.256 ps. For a double pass configuration, a total time delay is calculated to be 4.512 ps. This is equivalent to an optical path difference of 1353 μm. The advantage of the RSOD is evident here since this 1354 μm optical path difference corresponds to 1354 μm of linear mechanical movement of the linear actuator, but in the RSOD it only causes the edge of the galvanometer mirror to travel about 50 μm. This enables a much faster and stable scanning. During imaging, a saw tooth waveform is used to drive the galvanometer mirror.

Reference Arm

The configuration of the reference arm is shown as below. RSOD is the same as illustrated in the previous section. The only difference is that the light diffracted off the grating, goes through an off-centered focal lens. Light will reflect off the scanning mirror and go back along a different optical path. This off-centered setup will make sure that after reflecting of the galvanometer for the first time, the beam will incident on mirror 2 instead of going back to the fiber coupler. Mirror 2 is placed at a correct angle to catch this light beam and reflect it back to the RSOD and then coupled back into the fiber. The design actually increased the optical path length without further increasing the total area the reference occupies and enabled the entire system to be more compact and more available in field practice.

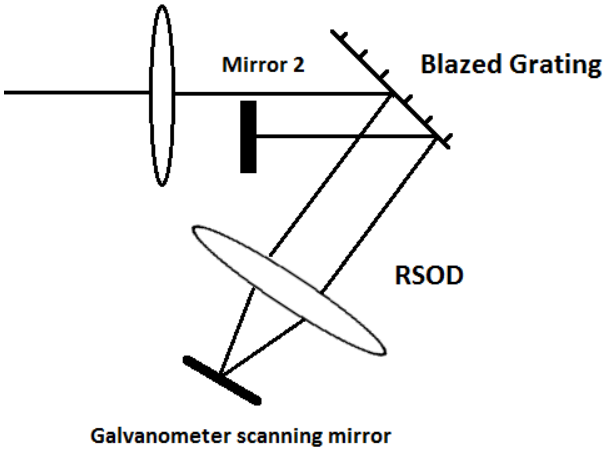

Figure 12. Schematic of the reference arm

EO Phase Modulator

An electro-optic modulator (EOM) is a device employing the electro-optic effect to modulate the phase of the light signal. The electro-optic effect is the change of the material optical property (usually crystal material) in response of an external electric field. At the atomic level, an external electric field applied to the crystal will cause a redistribution of bond charges and a slight deformation of the crystal lattice. These deformations are usually not isotropic and they varies according to the direction in the crystal. Crystals lacking a center of symmetry will exhibit a linear electro-optic effect, also known as Pockels effect [37]. As the electric field varies, the refractive index of the crystal changes. The phase of light leaving the crystal is proportional to the amount of time for the light to travel through it. As the refractive index changes, this time also changes which mean the phase is controlled by the electric field applied to the crystal. Assuming the light

entering the EOM is expressed as $\mathrm{Ae}^{\mathrm{iwt}}$. A sinusoidal electric field is applied to the EOM and the result signal becomes

$$\mathrm{Ae}^{\mathrm{iwt+ir*sin(ft)}} \tag{28}$$

here r is the amplitude and f is the frequency of the sine wave. If r is small, equation 28 becomes

$$\mathrm{Ae}^{\mathrm{iwt}} * (1 + \mathrm{ir} * \sin(\mathrm{ft})) = A(e^{iwt} + \frac{\mathrm{r}}{2} * \mathrm{e}^{\mathrm{i(w+f)t}} - \frac{\mathrm{r}}{2} * \mathrm{e}^{\mathrm{i(w-f)t}}) \tag{29}$$

In our setup, a lithium niobate modulator is used to modulate the light in the reference arm. This modulation creates an additional frequency shift apart from the frequency shift generated by scanning the galvanometer in reference arm and either the higher or the lower of the modulation frequency can be chosen to enable the heterodyne detection [27].

Object Arm

The object arm of our OCT system is similar to a conventional confocal microscopy in which the optical fiber also serves as a pinhole. Because of the size limitation of the scanning mirror, the light coming out of the optical fiber first goes through a preliminary focusing lens to focus the beam onto the scanning micromirror. Light reflects off the scanning mirror and enters the primary objective lens and focuses onto the sample under imaging.

The basic principle of confocal microscopy is illustrated in figure 13. It explains how the signal is acquired at one point on the sample. The incident light passing through the pinhole is focused on the sample at the focal plane. The light reflected from the sample is

collected by the lens and propagates back to the pinhole. If the sample is out of focus, the reflected light will be blocked by the pinhole and will not be detected by the photodetector after the pinhole. By raster scanning the sample or the light spot a 2D image can be obtained. More importantly, if we deliberately move the sample along the incident direction, the light spot will focus at a different depth in the sample. This information is essentially the depth information of the sample. Combined with the sample raster scanning, a 3D image of the sample can be obtained.

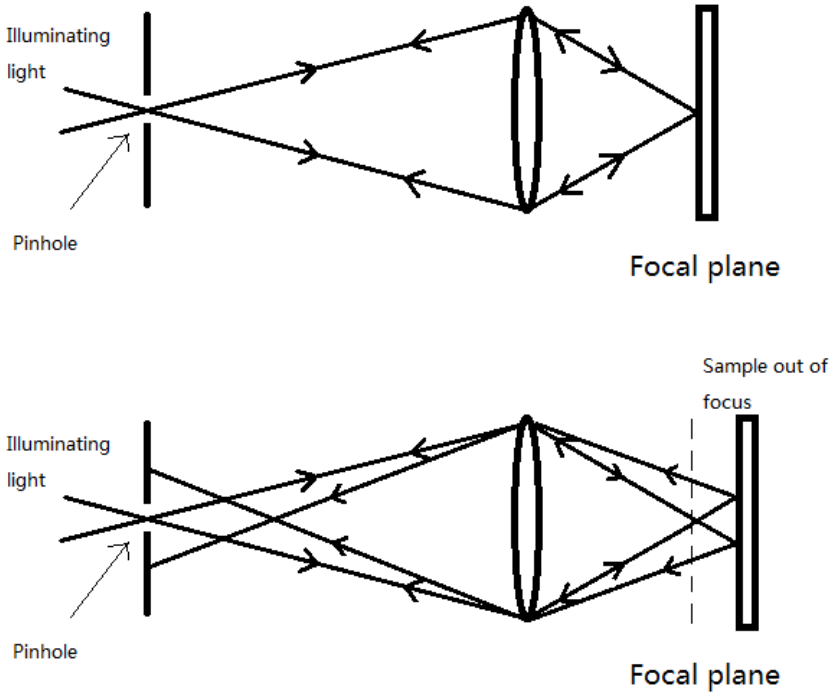

Figure 13. Confocal microscopy illustration

In our setup, the light is coupled into the sample arm by an optical fiber. One lens (lens 1) is used to focus the light onto the mirror and the second lens (lens 2) serves as the primary objective lens to focus light onto sample. It is worth noting that the optical fiber also

serves as the pinhole. Only light coming from the focal point will be coupled back into the fiber and be detected.

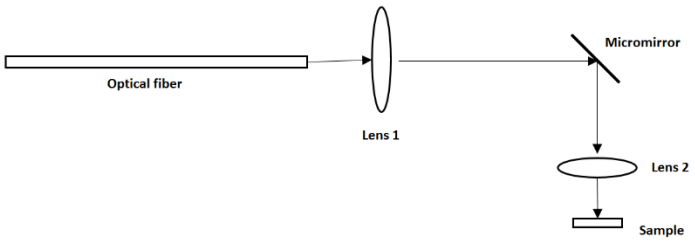

Figure 14. Schematic of object arm, lens 1 has a very long focal length and is used to focus as much light as possible onto the MEMS micromirror to avoid loss

Here Lens 2 is a bi-convex lens with a focal length of 30 mm and a diameter of 10 mm. Using equation 14, the minimum lateral resolution can be approximated to be 4.8 µm.

Photodetection

The photodetection is accomplished by detecting the interference signal with a Newport 818-IR germanium photodiode detector and feeding photocurrent into a Newport 1830-C optical power meter. Theory predicts that the photodiode noise is largely thermal (Johnson) noise associated with the effective resistance of the photodiode [38]. Johnson noise in photodetector is described as

$$\mathrm{I_{Johnson}} = \mathrm{sqrt}\left(\frac{4*\mathrm{kTB}}{\mathrm{R_{sh}}}\right)\ [A] \tag{30}$$

where k = $1.38*10^{-23} m^2\ kg\ s^{-2}\ K^{-1}$ is Boltzmann constant, T is temperature in Kelvin, B is bandwidth and R_{sh} is the shunt resistant. In 818 series, the shunt resistance is 50 kΩ. This gives a Johnson noise current of about 50 pA at 10 kHz bandwidth. Such a noise level is

sufficiently small for our purpose. Additionally, this power meter has a built-in transimpedance current amplifier to convert current from the photodetector to voltage and a voltage amplifier of X1 or X10. The amplification is associated with auto range function which adjusts the output signal level based on input level. Note that auto range function needs to be turned off when acquiring images to avoid artifacts.

3.6 Dispersion Management

Due to the requirement for a better axial resolution, a broadband laser source is usually desired in an OCT system. However such a broadband light source introduces an undesired effect: chromatic dispersion. Chromatic dispersion is associated with the frequency dependence of refractive index thus it is a material characteristic and it cannot be avoided but only reduced or balanced. From figure 15 we can see that for a material like fused silica, at longer wavelength, the refractive index is smaller.

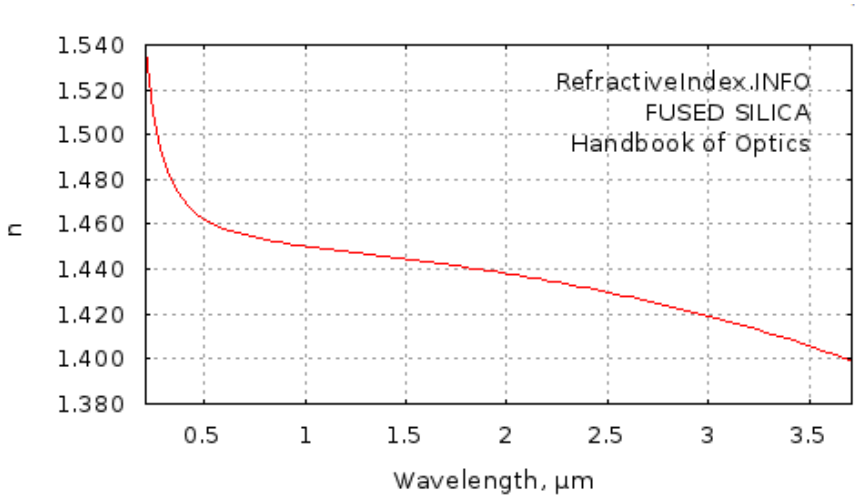

Figure 15. Fused silica refractive index [41]

In time domain, the electric field intensity in lateral direction can be expressed as

$$\mathbf{E}(\mathbf{r},\mathbf{t}) = \frac{1}{2}[\mathrm{E}(\mathrm{r},\mathrm{t}) * \mathrm{e}(-\mathrm{i} * \mathrm{wo} * \mathrm{t})] * \boldsymbol{x} \tag{31}$$

Converting it to frequency domain, we have

$$\mathbf{E}(\mathbf{r},\mathrm{w}-\mathrm{wo}) = \mathrm{F}(\mathrm{x},\mathrm{y}) * \mathrm{A}(\mathbf{z},\mathrm{w}-\mathrm{wo}) * \mathrm{e}^{\mathrm{i}\beta\mathbf{z}} \tag{32}$$

Here F(x,y) is the field distribution and A(z, w-w_o) is the variation of E-field along propagation direction and β is the propagation constant. The term $e^{i\beta z}$ is the change of phase φ(w). The temporal shape A(z, t) can be obtained by inverse Fourier transform.

$$\mathrm{A}(\mathbf{z},\mathrm{t}) = \frac{1}{2\pi}\int_{-\infty}^{\infty} A(\boldsymbol{z}, w-wo)e^{i\varphi(\mathrm{w})}e^{-i(w-wo)t}dw \tag{33}$$

Now assuming the optical signal propagates over a length of L, the total phase change is then

$$\varphi(\mathrm{w}) = 2\pi\mathrm{n}(\mathrm{w})\frac{\mathrm{L}}{\lambda} = wn(w)\frac{L}{c} \tag{35}$$

where n(w) is refractive index and c is speed of light in vacuum. If we expand this phase change using Taylor series, we have

$$\varphi(\mathrm{w}) = \varphi\mathrm{o} + \frac{\mathrm{d}\varphi}{\mathrm{dw}}(w-wo) + \frac{1}{2}\frac{(d^2\varphi)}{dw^2}(w-wo)^2 + \frac{1}{6}\frac{d^3\varphi}{dw^3}(w-wo)^3 + \cdots \tag{36}$$

Plug equation 36 back into equation 33 is it clear to see that the first term, sometimes also called zero-order term, φo in Taylor expansion does not affect the temporal shape. It corresponds to a constant phase shift. The first order term $\frac{\mathrm{d}\varphi}{\mathrm{dw}}(w-wo)$ also has no effect on temporal shape since from equation 35, $\frac{\mathrm{d}\varphi}{\mathrm{dw}} = \frac{n}{c}\left(1 + \frac{w}{n} * \frac{dn}{dw}\right)L = L * \frac{dk}{dw} = \frac{L}{vg}$ where vg is the group velocity by definition. The result $\frac{L}{vg}$ can be viewed as a time constant for the wave to travel distance L with the group velocity vg. The third term, and fourth

term, also called the 2nd order dispersion and 3rd order dispersion, do have an effect on the temporal shape of the wave.

Group velocity is also defined as $v_g=\frac{c}{N}$, where $N = (1 + \frac{\lambda}{n} * \frac{dn}{d\lambda})$ is the group index. Since the wavelength dependent refractive index can be obtained for both lithium niobate and fused silica optical fiber, it is more convenient to calculate dispersion using group index. Expand group index using Taylor and taking the 2nd order term out of the result, the 2nd order dispersion of the material per unit length is

$$\frac{d^2\varphi}{dw^2} = \frac{\lambda}{c*wo} * (\frac{d\left(\frac{\lambda}{n}\left(\frac{dn}{d\lambda}\right)\right)}{d\lambda}) \quad (38)$$

The third order dispersion of the material per unit length is

$$\frac{d^3\varphi}{dw^3} = -\frac{wo^4}{4\pi^2c^3}(3 * \frac{d^2n}{d\lambda^2} + wo * \frac{d^3n}{d\lambda^3}) \quad (39)$$

For RSOD, the dispersion is calculated as follows [30],

$$\frac{d^2\varphi}{dw^2} = -16 * \frac{\pi^2 c}{wo^3} * \frac{1}{d^2*\cos^2\theta\_\lambda}(L - f)(1 - \Delta\theta) \quad (40)$$

$$\frac{d^3\varphi}{dw^3} = 48 * \pi^2 * \frac{c(L-f)}{d^2*wo^2*\cos^2\theta_\lambda}\left[1 + \frac{\left(tan\theta_\lambda + \frac{1}{3}\Delta\theta\right)(2*\pi c)}{wo*d*cos\theta_\lambda}\right] + 192 * \frac{\pi^3c^2f}{d^3w\,o^{5\cos^3\theta_\lambda}}\Delta\theta \quad (41)$$

At 1.325 µm wavelength, the 2nd and 3rd order dispersion is calculated as

Optical Component	LiNbO3 (per mm)	RSOD per mm (L-f)	Fiber (per mm)
ϕ '' (fs2)	181.4	-403.6	-4.61
ϕ ''' (fs3)	298.15	904.4	84.4

Lithium Niobate crystal length is approximately 70 mm. It can be calculated that an L-f of 8.6 mm is needed to compensate for up to 2nd order with an extra fiber of 750 mm and without the EO modulator. Ideally, 78 mm L-f and an extra optical fiber of 666 mm is needed to compensate for up to third order dispersion with the EO modulator.

Chapter 4 Imaging Procedure and Results

4.1 Reference Arm Characterization

The characterization of reference arm of a TD-OCT is an important step for acquiring interference signal. In TD-OCT, the depth information is obtained by varying the reference arm optical path length through an RSOD component. For a well-characterized system (Figure 16), light coming out of the coupler A will incident on Mirror C and reflect to the blazed grating D. The 1st order diffraction will go through lens E eccentrically and incident on the galvanometer positioned at the focal plane of the lens. The reflecting beam will go through the lens E again and back to the grating then to mirror C. Because incoming beam does not go through the center of lens E, instead of traveling back to coupler A, the 1st return beam will incident on mirror B placed below A. B is adjusted so that the light reflects off it will follow the exact same path back in the order of C->D->E->F->E->D->C->A. This is the double pass configuration. A good alignment will produce little signal variation during the scanning of galvanometer thus preserve interference signal for deeper depth, or longer optical path length change.

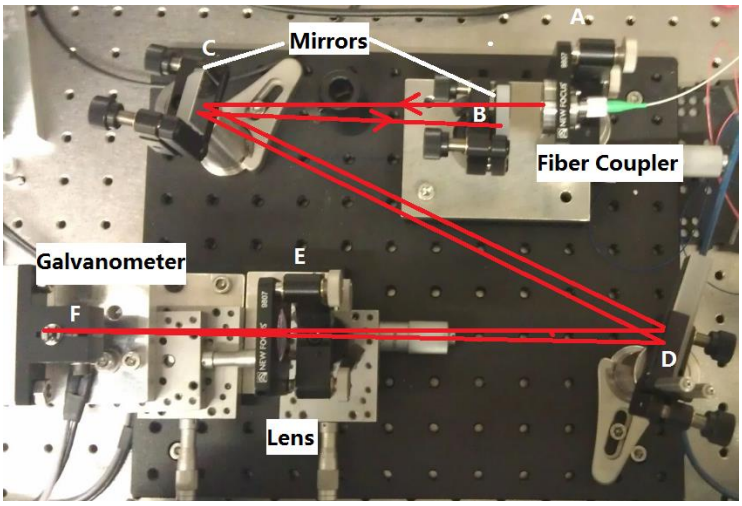

Figure 16. Illustration of the reference arm, A, Fiber coupler, B, C, Mirror, D, Grating, E, Lens and F, Galvanometer

Figure 17 shows a signal received from reference arm at 0V, 0.2 V, 0.5 V and 1 V galvanometer actuation voltage. Since in our setup, 1V in galvanometer is capable of producing more than 1 mm of scan depth, we will use it as a standard to judge the alignment of the reference arm. When F is at the focal plane of E, the A good alignment will produce small fluctuation even at large galvanometer deflection angle.

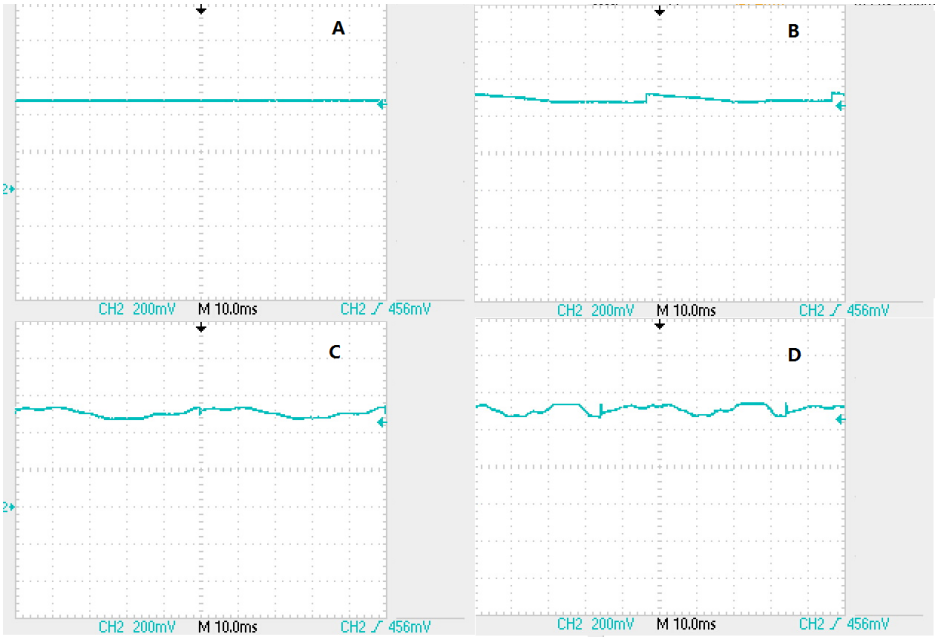

Figure 17. Reference Arm signals at A (0V), B (0.2V), C (0.5V) and D (1V). Signal level is constant at 456 mV under all actuation voltage

Since the RSOD employs a grating to separate different frequency components, it is also impossible to inspect the alignment quality by inspecting the frequency distribution of the beam.

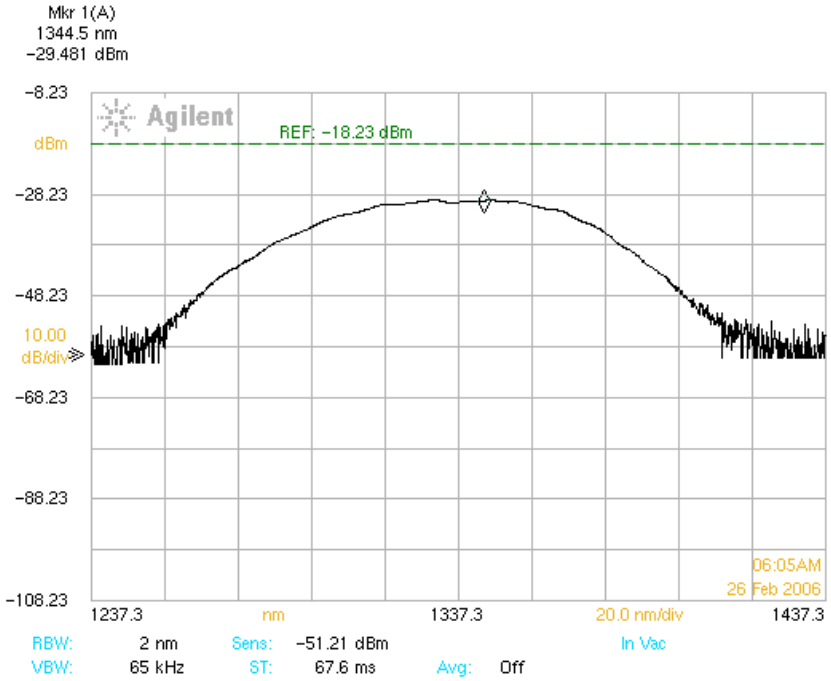

Figure 18. Spectrum of the light source before RSOD

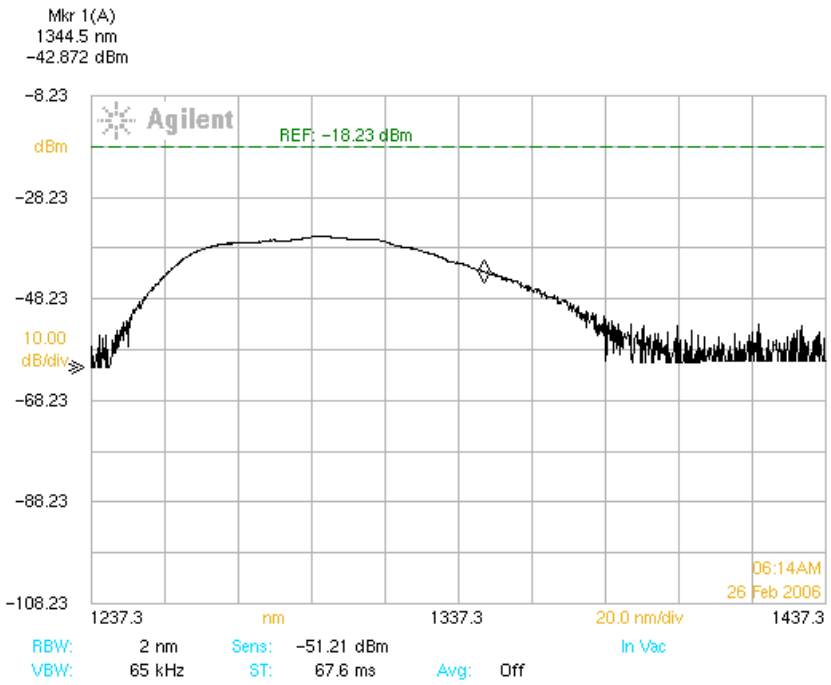

Figure 19. Spectrum of light source after RSOD

Figure 18 and 19 show the spectrum of the light before and after the RSOD. It can be seen that after RSOD, the spectrum is slightly distorted at lower frequencies. This will create an intensity artifact for the depth imaging since at different depths the signal is actually weighted differently. This effect is however, not substantial. Also it is worth noting that the actual FWHM of the light source is larger than 100 nm specified by the laser diode manufacturer due to the fact that we are biasing the diode at a higher current rating.

4.2 Object Arm Characterization and Confocal Imaging

The object arm setup is analogous to a confocal microscopy. A bi-convex object lens with a focal length of 30mm is used (Figure 20). The imaging target is placed at the focal point of the object lens. The MEMS scanning mirror is also placed at the focal point on the other side of the lens. Since the beam is collimated and narrow compared to lens diameter, ray approximation indicates that as the incident beam scans, the reflection beam will travel

back to the mirror. In reality however, only using a telecentric lens will ensure that at all scanning angle, the beam will focus on the same focal plane. This can be achieved using a microscopy object lens as most of these lenses are designed to be telecentric [26]. The target used for testing the spatial imaging and lateral resolution is a series of square checker board patterns.

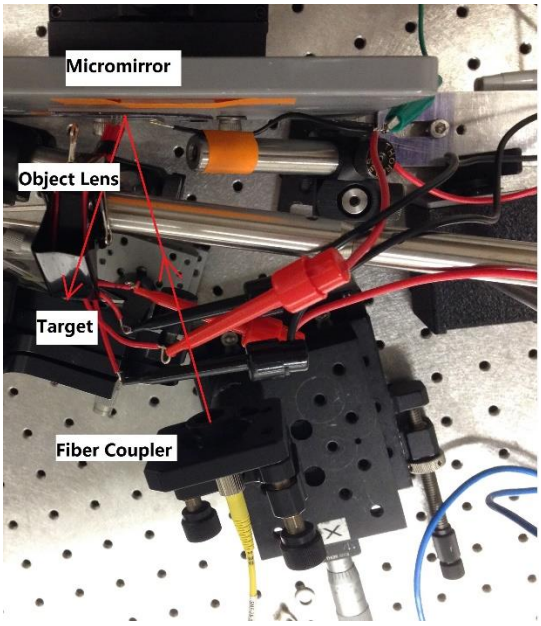

Figure 20. Illustration of the object arm

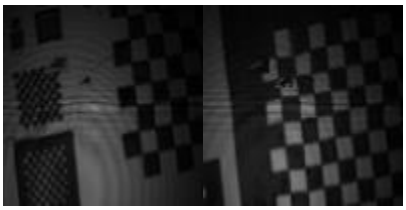

Figure 21. Right, 200 µm (each bright/dark square) pattern. Left, 200, 50, 20, 10, 5 µm pattern. The entire target is fabricated on a silicon wafer. The bright regions are aluminum and dark regions are black silicon.

The Object arm confocal setup is able to resolve 200 and 50 µm pattern. The image shows some level of distortion due to the nonlinearity of the micromirror tilting angle with voltages.

4.3 Interference and Depth Imaging

Without EO modulator, interference is achieved with a free space distance of 270 mm at the object arm. The reflectance of the MEMS scanning mirror is measured to be 98% at 1325 nm. Using the same material as target, an interference image is obtained for a galvanometer frequency of 1 Hz at 1 volt which corresponds to about 1.39 mm depth based on previous calculation and galvanometer specification.

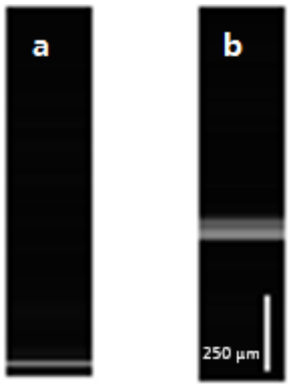

Figure 22. 1D depth images for a gold coated mirror surface (A-scan only) for 1V galvanometer scanning. Left, zero position, right, 25 µm further away from zero position

Since at 1325 nm, for 200 nm of gold layer thickness, 97.7% light will reflect off the surface, only one bright layer is seen. Figure 22.a is take when the gold target is at a set initial position. Figure 22.b is taken when sample is moved away by 50.8 µm. This shows that the real depth of imaging is about 1.3 mm and the system is capable of acquiring signal at different depth. The measured scanning depth is very close to the theoretical value calculated in Sec. 3.4. Note the above images are A-scan only, i.e. there is no spatial scanning through MEMS mirror. The width of the picture is just an extended A-scan of one pixel. It shows fairly consistent result without external interference.

Figure 23. 1D depth image of a glass slide of thickness 140 µm.

Figure 23 is a depth image of a glass slide with a thickness of 140 µm. The two bright lines in the image are the front and back surface of the glass slide. The measured thickness of the slide from the image is in good agreement with the actual thickness. Here it is worth noting that the glass slide has a higher refractive index therefore a longer optical path length compared to air. This results in a longer distance in the image since OCT system does not account for refractive index change.

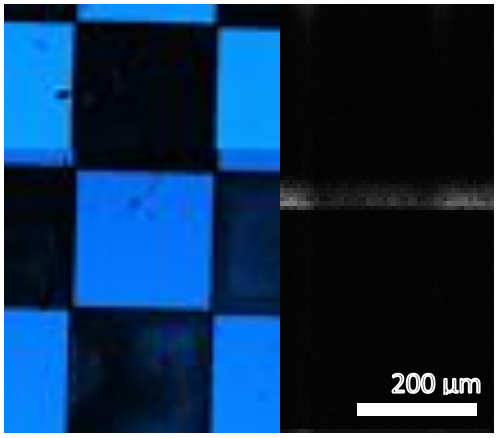

Figure 24. Right, 2D cross-sectional image of the checker board target. Left, microscope image

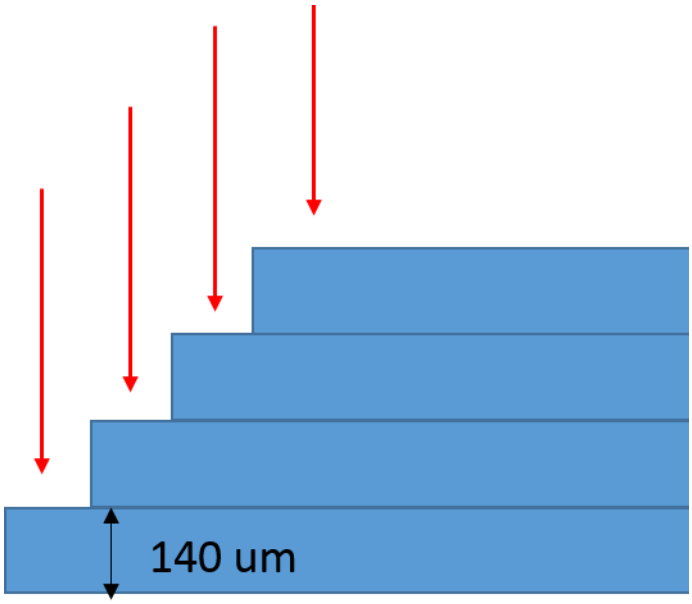

Figure 25. Schematic of the stacked glass slides

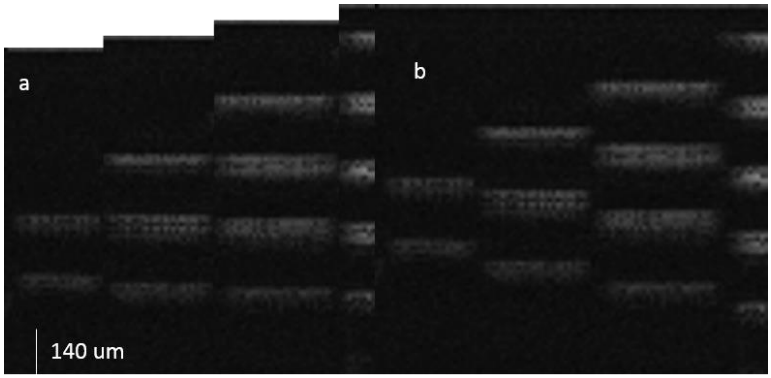

Figure 26. a depth compensated image, b. original image, of glass slides stack

The 2D cross-sectional images are obtained by scanning the MEMS micromirror laterally along one dimension. Figure 25 shows the cross-sectional image of the checker board pattern. The less bright area in the middle is the etched silicon since it is less reflective than the aluminum. Figure 26 shows the cross-sectional image of a stacked glass slides. Since glass has a high refractive index, for the same distance, air and glass will have different optical path length. Since the OCT system has no refractive information, it does not compensate for it. The result is layer mismatch in this glass stack image.

4.4 Dispersion Investigation

The effect of dispersion in the system is examined. In the current setup. Both the RSOD in the reference arm and the optical fiber in the object arm generate a positive dispersion. This means that higher frequency components propagate faster in the medium than lower frequency components. For example, a longer L-f than necessary will create more dispersion in the reference arm. Essentially higher frequency components will see a longer optical path length. As the galvanometer scans, different frequency components will interfere the same target depth at different moment. This means the axial resolution is degraded. Figure 27 shows two A-scan results of a same gold surface with dispersion mismatched on the left and dispersion matched up to 2nd order on the right. It is obvious that dispersion mismatch could be detrimental to axial resolution.

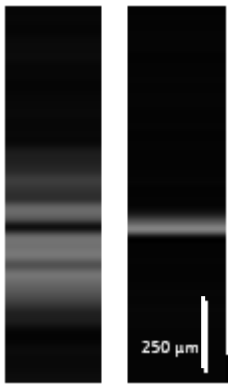

Figure 27. Left, Gold surface image with L-f=78 mm. Right, gold surface image with L-f = 8.6 mm

Note that without the EO modulator, it is impossible to compensate both the second and third order dispersion. Due to the fact that dispersion is compensated only up to second order in the current setup. Some level of degradation of the axial resolution is still expected.

Chapter 5 Conclusion

A time-domain optical coherence tomography system is demonstrated in combination with a MEMS micromirror scanner for sample lateral scanning. The system employs a rapid scanning optical delay line to acquire depth information as well as modulate the interference signal for heterodyne detection of the small inference signals as a result of low reflectivity of the samples. Interference signal is successfully achieved and the signal is processed through an active high-pass filter and an analog to digital convertor. Due to the lack of an envelope detector, the image frame rate and size are limited. Depth imaging ability is tested and the calculated and measured RSOD effects are in good agreement. 2D cross-sectional image is acquired using this system and the resulting axial resolution is investigated and discussed.

In the future, an effective envelope detector is needed to improve the performance of the system. Past literature shows that a fourth-order finite impulse response (FIR) filter with Hanning window is suitable for this application [40]. Additionally, an EO modulator can be employed to increase the modulation frequency and to better compensate the third order dispersion for optimal axial resolution. To obtain a 3D image, a third analog output is required. This is usually achieved by either a more advanced NI DAQ with more than two analog output or multiple DAQs synchronized.

Chapter 6 Major Components list

Cambridge Technology Model 6210H Optical Scanner

Thorlabs SLD1325 superluminescent diode (SLD) light source for OCT system.

Thorlabs Richardson 53*500R blazed grating with aluminum coating.

EO Space PM-DV5-40-PFA-PFA-130, 40 Gb/s lithium niobate phase modulator 1300nm

4V Vp at 1GHz 5dB insertion loss.

ST MC1485 Dual Operational Amplifier

Thorlabs LB1258, f=30mm, d=12.7 mm

National Instruments PCI-6024E Multifunction DAQ

Newport 1830-C power meter

Thorlabs SMC FC-FC optical fiber 750mm

Reference

[1] “Compton Scattering of X Rays from Bound Electrons”, P. Eisenberger and P.M. Platzman, Physical Review A, August 1970, Vol. 2, No. 2.

[2] “DNA Damage & Repair: Mechanisms for Maintaining DNA Integrity”, Suzanne Clancy, Nature Education 1(1):103, http://www.nature.com/scitable/topicpage/dna-damage-repair-mechanisms-for-maintaining-dna-344

[3] “Extended-Field–of-View Ultrasound Imaging”, Hand book of Medical Imaging, Kim, Yongmin; Horii, Steven C, Volume 3Display and PACS, Chapter 6, 278-281.

[4] “Magnetic Resonance Imaging”, David Pickens, Hand book of Medical Imaging: Physics and Psychophysics, chapter 6, 417-418.

[5] “Introduction to Optical Coherence Tomography (OCT)”, University of Western Australia, Optical+Biomedical Engineering Laboratory, http://obel.ee.uwa.edu.au/research/oct/introduction-to-oct

[6] “Dynamic focus-tracking MEMS scanning micromirror with low actuation voltages for endoscopic imaging”, Matthew Strathman, Yunbo Liu, Xingde Li and Lih Y. Lin, OPTICS EXPRESS, October, 2013, Vol. 21, No. 20.

[7] “Prototype scanning fiber endoscope”, Eric J. Seibel, Quinn Y.J. Smithwick, Janet L. Crossman-Bosworth, John A. Myers, Proceedings of SPIE, March, 2002, Vol. 4616.

[8] “3D *In Vivo* optical coherence tomography based on a low-voltage, large-scan-range 2D MEMS mirror”, Huikai Xie et.al, Optics Express, May, 2010, Vol. 18, No.12.

[9] “Two-axis MEMS Scanning Catheter for Ultrahigh Resolution Three-dimensional and *En Face* Imaging”, Aaron D. Aguirre, Paul R. Herz, Yu Chen, James G. Fujimoto, Optics Express, March, 2007, Vol. 15, No. 5.

[10] “Rapid-scanning forward-imaging miniature endoscope for real-time optical coherence tomography”, X. Liu, M. J. Cobb, Y. Chen, M. B. Kimmey, and X. Li, Opt. Letters, August, 2004, Vol. 29, No. 15.

[11] "Integrated multimodal endomicroscopy platform for simultaneous en face optical coherence and two-photon fluorescence imaging", J. F. Xi, Y. P. Chen, Y. Y. Zhang, K. Murari, M.-J. Li, and X. D. Li, Opt. Letters, February, 2012, Vol. 37, No. 3.

[12] “Scanning fiber endoscopy with highly flexible, 1 mm catheterscopes for wide-field, full-color imaging”, C. M. Lee, C. J. Engelbrecht, T. D. Soper, F. Helmchen, and E. J. Seibel, J. Biophotonics, June, 2010, Vol. 3, No. 5-6.

[13] "Fiber-optic scanning two-photon fluorescence endoscope", M. T. Myaing, D. J. MacDonald, and X. D. Li, Opt. Letters, April, 2006, Vol. 31, No. 8.

[14] "A compact fiber-optic SHG scanning endomicroscope and its application to visualize cervical remodeling during pregnancy", Y. Zhang, M. L. Akins, K. Murari, J. F. Xi, M.-J. Li, K. Luby-Phelps, M. Mahendroo, and X. D. Li, Proceedings of the National Academy of Sciences, July, 2012, Vol. 109.

[15] “Handbook of Medical Imaging Volume III”, Arun Tirumalai, Carol Lowery, David Gustafson, Pat Sutcliffe, Pat VonBehren, Chapter 6, 278-285.

[16] “MOEMS 3D scan mirror for single-point control of beam deflection and focus”, Yuhe Shao, David L. Dickensheets, J. Microlith., Microfab., Microsyst., October, 2005, Vol. 4(4), No. 04150.

[17] “Submillimeter Optical Reflectometry”, H. H. Gilgen, R. P. Novak, R. P. Salathe, W. Hodel and P. Beaud, Journal of Lightwave Technology, August, 1989, Vol. 7, No. 8.

[18] “Optical Coherence Tomography”, David Huang, Eric A. Swanson, Charles P. Lin, James G. Fujimoto et al, Science, November, 1991, Vol. 254, No. 5035.

[19] “Optical coherence tomography”, James G. Fujimoto, Applied Physics, July, 2001, Vol. 4.

[20] “Optical Coherence Tomography---Principles and Applications”, A. F. Fercher, W. Drexler, C. K. Hitzenberger and T. Lasser, Rep. Prog. Phys., January, 2003, Vol. 66.

[21] “Theory of Optical Coherence Tomography”, Optical Coherence Tomography, Technology and Applications, J.A. Izatt and M.A. Choma, Chapter 2, 52-54.

[22] “Principle of Optics”, M. Born and E. Wolf. Chapter 8.5, 395-398.

[23] “Application of Apodization to Increase Two-point Resolution by The Sparrow Criterion. I. Coherent Illumination”, Richard Barakat, 1962 Journal of the Optical Society of America, Vol. 52, No. 3.

[24] “Theory of Optical Coherence Tomography”, Optical Coherence Tomography, Technology and Applications, J.A. Izatt and M.A. Choma, Chapter 2, 49-50.

[25] “Optical Coherence Tomography (OCT) A Review”, Joseph M. Schmitt, IEEE Journal of Selected Topics in Quantum Electronics, July/August, 1999, Vol. 5 No. 4.

[26]”Confocal Scanning Optical Microscopy and Related Imaging Systems”, Timothy R. Corle and Gordon S. Kino, Chapter 2.2, 76-77.

[27] “Optical heterodyne detection”, O. E. DeLange, IEEE Spectrum, October, 1968, Vol. 5, Issue 10.

[28] “Optical Coherence Tomography”, James G. Fujimoto et.al. Science, New series, November, 1991, Vol. 254, No. 5035, 1178-1181.

[29] “Dispersion management up to the third order for real-time optical coherence tomography involving a phase or frequency modulator”, Yuchuan Chen and Xingde Li, Optics Express, November, 2004, Vol. 12, No. 24.

[30] “RC Active Filter Design Handbook”, Stephenson, F. W., Chapter 2.4, 26-29.

[31] “High-speed phase- and group-delay scanning with a grating-based phase control delay line”, G. J. Tearney, B. E. Bouma, and James G. Fujimoto, Opt. Letters, December 1, 1997, Vol. 22, No. 23.

[32] “400-Hz mechanical scanning optical delay line”, K.F. Kwong, D. Yankelevich, K.C. Chu, J.P. Heritage, and A. Dienes. April, 1993, Opt. Letters, Vol. 18, No.7.

[33] “Picosecond pulse shaping by spectral phase and amplitude manipulation”, J. P. Heritage, A. M. Weiner, and R. N. Thurston, Opt. Letters, December 1985, Vol. 10, No. 12.

[34] “Analysis of Picosecond Pulse Shape Synthesis by Spectral Masking in a grating Pulse Compressor”, R. N. Thurston, J. P. Heritage, A. M. Weiner, and W. J. Tomlinson, IEEE J. Quantum Electron, May 1986, Vol. QE-22, No. 5.

[35] “Picosecond and Femtosecond Fourier Pulse Shape Synthesis”, A. M. Weiner and J. P. Heritage, Rev. Phys. Appl., December, 1987, Vol. 22, No. 12.

[36] “High-resolution Femtosecond Pulse Shaping”, A. M. Weiner, J. P. Heritage, and E. M. Kirschner, J. Opt. Soc. Am., August, 1988, Vol. 5, No. 8.

[37] “Handbook of Optics, Volume II”, Theresa A. Maldonado and Michael Bass, Chapter 13, 13.3-13.14.

[38] “818 Series Photodetector Guide”, Newport Corporation, http://assets.newport.com/webDocuments-EN/images/RevB_818_Series_Manual.pdf

[39] “Handbook of Optics, Volume IV”, Michael Bass, Casimer DeCusatis, Jay Enoch,Vasudevan Lakshminarayanan, Guifang Li, Carolyn MacDonald, Virendra Mahajan, Eric Van Stryland.

[40] “Signal Processing in optical coherence tomography for aerospace material characterization”, Ping Liu and Roger M. Groves, Optical Engineering, March, 2013, Vol. 52, No. 3.

[41] “Optical constants of fused silica”, Handbook of Optics, http://refractiveindex.info/legacy/?group=GLASSES&material=F_SILICA